

# Detection of 21-cm, H<sub>2</sub> and Deuterium absorption at $z > 3$ along the line-of-sight to J1337+3152<sup>\*</sup>

R. Srianand<sup>1†</sup>, N. Gupta<sup>2</sup>, P. Petitjean<sup>3</sup>, P. Noterdaeme<sup>1</sup> & C. Ledoux<sup>4</sup>

<sup>1</sup> IUCAA, Postbag 4, Ganeshkhind, Pune 411 007, India

<sup>2</sup> Australia Telescope National Facility, CSIRO, Epping, NSW 1710, Australia

<sup>3</sup> Université Paris 6, UMR 7095, Institut d'Astrophysique de Paris-CNRS, 98bis Boulevard Arago, 75014 Paris, France

<sup>4</sup> European Southern Observatory, Alonso de Córdova 3107, Casilla 19001, Vitacura, Santiago 19, Chile

Accepted. Received; in original form

## ABSTRACT

We report the detection of 21-cm and molecular hydrogen absorption lines in the same damped Lyman- $\alpha$  system (with  $\log N(\text{H I})=21.36\pm 0.10$ ) at  $z_{\text{abs}}=3.17447$  towards SDSS J133724.69+315254.55 ( $z_{\text{em}} \sim 3.174$ ). We estimate the spin temperature of the gas to be,  $T_{\text{S}} = 600^{+222}_{-159}$  K, intermediate between the expected values for cold and warm neutral media. This suggests that the H I absorption originates from a mixture of different phases. The total molecular fraction is low,  $f_{\text{H}_2}=10^{-7}$ , and H<sub>2</sub> rotational level populations are not in equilibrium. The average abundance of the  $\alpha$ -elements is,  $[\text{S}/\text{H}]=-1.45 \pm 0.22$ . Nitrogen and iron are found underabundant with respect to  $\alpha$ -elements by  $\sim 1.0$  dex and  $\sim 0.5$  dex respectively. Using photoionization models we conclude that the gas, of mean density,  $n_{\text{H}} \sim 2 \text{ cm}^{-3}$ , is located more than 270 kpc away from the QSO. While the position of 21-cm absorption line coincides with the H<sub>2</sub> velocity profile, its centroid is shifted by  $\sim 2.7 \pm 1.0 \text{ km s}^{-1}$  with respect to the redshift measured from the H<sub>2</sub> lines. However, the position of the strongest metal absorption component matches the position of the 21-cm absorption line within  $0.5 \text{ km s}^{-1}$ . From this, we constrain the variation of the combination of fundamental constants  $x = \alpha^2 G_{\text{p}}/\mu$ ,  $\Delta x/x = -(1.7 \pm 1.7) \times 10^{-6}$ . This system is unique as we can at the same time have an independent constrain on  $\mu$  using H<sub>2</sub> lines. However, as the H<sub>2</sub> column density is low, only Werner band absorption lines are seen and, unfortunately, the range of sensitivity coefficients is too narrow to provide a stringent constraint:  $\Delta\mu/\mu \leq 4.0 \times 10^{-4}$ . The Ultraviolet and Visual Echelle Spectrograph (UVES) spectrum reveals another DLA at  $z_{\text{abs}}= 3.16768$  with  $\log N(\text{H I}) = 20.41 \pm 0.15$  and low metallicity,  $[\text{Si}/\text{H}] = -2.68 \pm 0.11$ , in which  $[\text{O}/\text{C}] \sim 0.18 \pm 0.18$  and  $[\text{O}/\text{Si}] \sim 0$ . This shows that even in the very early stages of chemical evolution, the carbon or silicon to oxygen ratios can be close to solar. Using Voigt profile fitting we derive  $\log(N(\text{D I})/N(\text{H I})) = -(4.93 \pm 0.15)$  in this system. This is a factor of two smaller than the value expected from the best fitted value of  $\Omega_{\text{b}}$  from the Wilkinson Microwave Anisotropy Probe (WMAP) 5 year data. This confirms the presence of astration of deuterium even at very low metallicity.

**Key words:** Galaxies: abundances – Quasars: absorption lines – Quasars: individual: SDSS J133724.69+315254.55

## 1 INTRODUCTION

Damped Lyman- $\alpha$  systems (DLAs) are the highest H I column density absorbers seen in QSO spectra, with  $N(\text{H I}) \geq 10^{20} \text{ cm}^{-2}$ , over cosmological time-scales. These absorbers trace the bulk of neutral hydrogen at  $2 \leq z \leq 3$  (for example see, Noterdaeme et al. 2009b) and have long been identified as revealing the interstellar medium of the high-redshift precursors of present day galaxies (for a review see, Wolfe et al.

<sup>\*</sup> Based on observations carried out at the European Southern Observatory (ESO), under programmes 082.A-0544 and 083.A-0454 (PI: C. Ledoux) with the UVES echelle spectrograph installed at the ESO Very Large Telescope (VLT), unit Kueyen, on Mount Paranal in Chile

<sup>†</sup> E-mail: anand@iucaa.ernet.in

2005). The physical conditions in the diffuse interstellar gas are influenced by a number of physical processes including in-situ star-formation, cosmic ray interaction, photoelectric heating by dust as well as mechanical energy input from both impulsive disturbances like supernova explosions and steady injection of energy in the form of stellar winds. Therefore, studies of the physical conditions in DLAs provide a probe of the cosmological evolution of normal galaxies selected solely based on H I cross-section.

Our understanding of physical conditions in DLAs is primarily derived from optical absorption-line studies, involving the detection of low-ionization metal transitions and, in some cases, molecular absorption [e.g. Petitjean et al. (2000), Ledoux et al. (2003) and Noterdaeme et al. (2008a), for H<sub>2</sub>, and Srianand et al. (2008) and Noterdaeme et al. (2009a) for CO]. The gas in which H<sub>2</sub> is detected, has typical temperature and density of  $150 \pm 80$  K and  $n_{\text{H}} = 10\text{--}200$  cm<sup>-3</sup> respectively. These conditions correspond to those prevailing in a cold neutral medium (CNM) embedded in a radiation field of moderate intensity originating from local star formation activity (Srianand et al. 2005).

Detecting 21-cm absorption in DLAs is one complementary way to probe the physical conditions in the absorbing gas. If detected, the 21-cm optical depth, in conjunction with the observed  $N(\text{H I})$  from optical data, gives the spin temperature of the H I gas (see Kanekar & Chengalur 2003). It is widely believed that the latter is a good tracer of the kinetic temperature. The width of the 21-cm line observed at very high spectral resolution can also yield a direct measurement (or give a stringent upper limit on) of the kinetic temperature (as, for example, in the  $z_{\text{abs}} = 1.3603$  system towards J 2340–0053, Gupta et al. 2009). This can be combined with measurements of C I, C II, Si II and/or O I fine-structure lines to derive the gas density (Heinmüller et al. 2006).

By measuring the relative positions of absorption lines it is possible to constrain the time variation of several dimensionless constants. Accurately measured wavelengths of H<sub>2</sub> absorption lines allow one to constrain the variation of the proton-to-electron mass ratio (Varshalovich & Levshakov 1993). The position of the 21-cm absorption line can be compared to those of the corresponding metal line components to probe the variations of a combination,  $x = \alpha^2 G_{\text{p}}/\mu$ , of the fine structure constant ( $\alpha$ ), the proton-to-electron mass ratio ( $\mu$ ) and the proton gyromagnetic factor ( $G_{\text{p}}$ , Tubbs & Wolfe 1980). Simultaneous detection of H<sub>2</sub>, 21-cm and metal absorption line in the same system can, in principle, allow one to lift part of the degeneracy between the variations of these different constants.

Despite obvious advantages, till recently, there was only one system (at  $z_{\text{abs}} = 1.7765$  towards Q 1331+170, Cui et al. 2005) known to produce both H<sub>2</sub> and 21-cm absorption lines. Due to the low redshift of the system, however, it is not possible to cover the H<sub>2</sub> Lyman and Werner band absorption with high resolution spectroscopy at high enough signal-to-noise ratio. This prevents one from performing a detailed analysis of the cloud. In the course of our on-going GBT/GMRT survey for 21-cm absorption in high- $z$  DLAs selected from the SDSS we discovered a DLA system, exhibiting both 21-cm and H<sub>2</sub> absorption lines, at  $z_{\text{abs}} = 3.17447$  towards J133724.69+315254.55 (called J 1337+3152 hereafter). This system is unique as both 21-

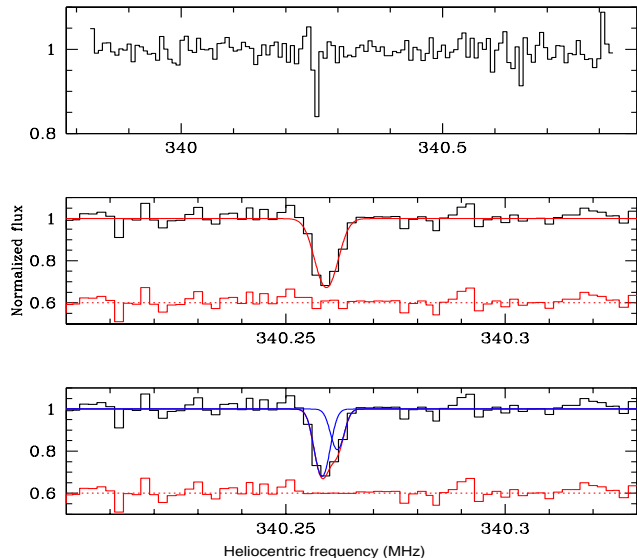


**Figure 1.** Normalised GMRT spectra showing the detection of  $z = 3.174480$  21-cm absorption toward J 1337+3152. *Top panel:* low resolution spectrum (6.88 km/s/channel) observed on January 13, 2009. *Middle and bottom panels:* high resolution spectrum (1.72 km/s/channel) together with, respectively, the best single or two gaussian component fit models. Residuals (shifted by 0.6 along the y-axis) are also shown.

cm absorption and H<sub>2</sub> are extremely rare in DLAs at  $z \geq 3$ . In addition, there is another DLA at  $z_{\text{abs}} = 3.16768$  along the same line-of-sight (at  $\sim 500$  km s<sup>-1</sup> away from the first DLA) with very low metallicity. In this paper, we present a detailed analysis of both DLAs.

## 2 DETAILS OF OBSERVATIONS

The quasar J1337+3158 was observed with the GMRT on January 13, 2009 to search for 21-cm absorption in the DLA at  $z_{\text{abs}} = 3.17448$ . Observations were performed in a bandwidth of 1 MHz split into 128 channels. We observed the nearby standard flux density calibrator 3C 286 every 45 minutes for the amplitude, phase and bandpass calibration. A total of 6.2 hrs of data were acquired on-source in both the circular polarization channels, RR and LL. Data were reduced using the NRAO Astronomical Image Processing System (AIPS) following standard procedures as described in Gupta et al. (2006). Special care was taken to exclude the baselines and timestamps affected by radio frequency interferences (RFI). An absorption feature confined in a single spectral resolution channel (6.88 km s<sup>-1</sup>) is detected consistently in both polarisations (see top panel of Fig. 1). In the Stokes I spectrum, the absorption corresponds to an integrated 21-cm optical depth,  $\int \tau dv = 1.55 \pm 0.19$  km s<sup>-1</sup>. The quasar was reobserved on March 17, 2009 during 7.8 hrs (on-source time) at a higher frequency resolution to confirm the 21-cm absorption. A bandwidth of 0.25 MHz split into 128 channels, i.e. a spectral resolution of 1.72 km s<sup>-1</sup>, was used. With respect to the first observing run, this second epoch observation corresponds to an overall shift in the observing frequency of 18.2 km s<sup>-1</sup> due to

the heliocentric motion of the Earth. The absorption profile was observed to be consistent with this velocity shift. We used AIPS task CVEL to correct the observed data for the Earth's motion and rotation. The higher resolution Stokes I spectrum (with rms of  $2.0 \text{ mJy beam}^{-1} \text{ channel}^{-1}$ ) from the second epoch observation together with the fits to the H I absorption are shown in the middle and bottom panels of Fig. 1.

We also observed J 1337+3152 with the Ultraviolet and Visual Echelle spectrograph (UVES; Dekker et al. (2000)) in visitor mode on March 27 and April 27, 2009. We used two settings with two different central wavelengths in the blue (390nm and 437nm) and red (600nm and 770nm) arms to cover the wavelength range 3300–9590 Å with a single gap between 7590 and 7769 Å. The CCD pixels were binned  $2 \times 2$  and the slit width adjusted to  $1''$ , yielding a resolving power of  $R = 45000$  under median seeing conditions of  $\sim 0''.9$ . The total exposure time on source is 4 hrs. The data were reduced using the UVES pipeline (Ballester et al. 2000), which is available in the context of the ESO MIDAS data reduction system. Wavelengths were rebinned to the heliocentric rest frame and individual scientific exposures co-added using a sliding window and weighting the signal by the inverse of the variance in each pixel. The resultant combined spectrum has a SNR in the range 10–20 per pixel. We fitted the quasar continuum using low order polynomials in line free continuum regions. We analysed the spectrum using standard Voigt profile fitting procedures. The atomic data used are from Morton (2003) unless otherwise specified. In the following, we adopt the solar photospheric abundances from Asplund et al. (2009), rest wavelengths and oscillator strengths of H<sub>2</sub> transitions from Ubachs et al. (2007) and Abgrall et al. (1994) respectively.

### 3 HIGH $N(\text{H I})$ SYSTEMS

There are three high- $N(\text{H I})$  absorption systems within  $2500 \text{ km s}^{-1}$  along this line of sight at  $z_{\text{abs}} = 3.17448$  ( $v = 0 \text{ km s}^{-1}$ ),  $3.16768$  ( $v = -488 \text{ km s}^{-1}$ ) and  $3.1408$  ( $v = -2420 \text{ km s}^{-1}$ ). The corresponding Lyman series absorption lines are shown on a velocity scale in Fig. 2. The Lyman- $\alpha$  profile is dominated by the  $z_{\text{abs}} = 3.17448$  system. As the red wing of this absorption is affected by the QSO Lyman- $\alpha$  emission, we do not use it to derive  $N(\text{H I})$  but use instead Lyman- $\beta$  and other higher order lines.

The Lyman- $\beta$  line of the  $z_{\text{abs}} = 3.17448$  and  $3.16768$  systems (referred to as system-1 and system-2 from now on) are blended together. Some of the higher order Lyman lines of system-1 are blended with lines from the sub-DLA at  $z_{\text{abs}} = 3.1408$  ( $\sim -2420 \text{ km s}^{-1}$ ). The main constraint on  $\log N(\text{H I})$  in system-1 comes from the red wing of the Lyman- $\beta$  absorption and the core of the Lyman- $\gamma$  absorption. In the case of system-2, the blue wing of Lyman- $\beta$  and the red wing of Lyman- $\gamma$  are used for the same purpose. We obtain  $\log N(\text{H I}) = 21.36 \pm 0.10$  and  $20.41 \pm 0.15$  for system-1 and system-2 respectively. Note that errors come mostly from continuum placement uncertainties. We discuss the fits to the H I lines for system-2 in greater detail below (see Sect. 5). In both cases, the unblended wings of the higher Lyman series lines are used to constrain the velocity dispersion.

In addition, based on the absence of damping wings in Lyman- $\beta$  and the blue wing of the Lyman- $\alpha$  absorption lines we derive an upper limit of  $10^{19} \text{ cm}^{-2}$  for  $N(\text{H I})$  at  $z_{\text{abs}} = 3.1408$  ( $\Delta v \sim -2420 \text{ km s}^{-1}$ ). We cannot perform a more precise measurement as all the available transitions are saturated, hiding the component structure. We therefore do not discuss this system any further.

### 4 ANALYSIS OF SYSTEM-1 ( $z_{\text{abs}} = 3.17448$ )

Weak H<sub>2</sub> and strong 21-cm absorptions are seen associated with this system in the UVES and GMRT spectra, respectively.

#### 4.1 21-cm absorption

The GMRT spectrum covers only the expected 21-cm range for system-1. In the higher resolution GMRT spectrum the absorption is spread over 7–8 channels and can be adequately fitted with a single Gaussian component of peak optical depth  $\tau = 0.40 \pm 0.02$  located at  $340.2593 \pm 0.0002 \text{ MHz}$  (or  $z_{\text{abs}} = 3.174480 \pm 0.000002$ ) and  $\text{FWHM} = 5.08 \pm 0.34 \text{ km s}^{-1}$  (see middle panel in Fig. 1).

The gaussian fit was carried out using an IDL code based on MPFIT, which performs  $\chi^2$ -minimisation by Levenberg-Marquardt techniques (Markwardt 2009). We use the rms flux measured in the line free channels as typical error in each channel. The best fit has a reduced  $\chi^2 = 1.02$ . The FWHM of the fitted Gaussian component corresponds to a kinetic temperature of  $T_{\text{K}} \leq 564 \pm 76 \text{ K}$ .

Motivated by the fact that the centroid of the H<sub>2</sub> absorption does not coincide with the centroid of the 21-cm absorption (see below), we performed a fit with two components. The result of this fit is shown in the bottom panel of Fig 1. The best fitted two components have  $z_{\text{abs}} = 3.174492 \pm 0.000007$  and  $3.174451 \pm 0.000012$  with  $\text{FWHM} = 3.4 \pm 0.9$  and  $3.1 \pm 1.6 \text{ km s}^{-1}$  respectively. These values translate to upper limits on kinetic temperatures of 252 and 210 K respectively. The reduced  $\chi^2$  in this case is 0.87. This, as well as the residuals seen in Fig. 1, suggest that the two component model is probably over-fitting the data.

The H I column density of an optically thin cloud covering a fraction  $f_c$  of a background radio source is related to the 21-cm optical depth  $\tau(v)$  in a velocity interval  $(v, v+dv)$  and to the spin temperature ( $T_s$ ) by

$$N(\text{H I}) = 1.835 \times 10^{18} \frac{T_s}{f_c} \int \tau(v) dv \text{ cm}^{-2}. \quad (1)$$

The total optical depth is  $\int \tau(v) dv = 2.08 \pm 0.17 \text{ km s}^{-1}$ . Thus the total H I column density is,  $N(\text{H I}) = (3.82 \pm 0.31) \times 10^{18} (T_s/f_c) \text{ cm}^{-2}$ . From our optical spectrum we measure  $\log N(\text{H I}) = 21.36 \pm 0.10$ . For  $f_c = 1$ , this yields  $T_s = 600_{-159}^{+222} \text{ K}$ . Interestingly this is very close to the upper limit we get from the width of the 21-cm absorption line for the single gaussian fit.

There is no milli-arcsecond scale resolution radio map available for the J 1337+3152 field. The radio source is compact in our GMRT images at 340 MHz with a resolution of  $10'' \times 8''$  and has a flux density of  $69.3 \text{ mJy}$ . In the VLA FIRST 1.4 GHz image (of resolution  $5'' \times 5''$ ) the radio

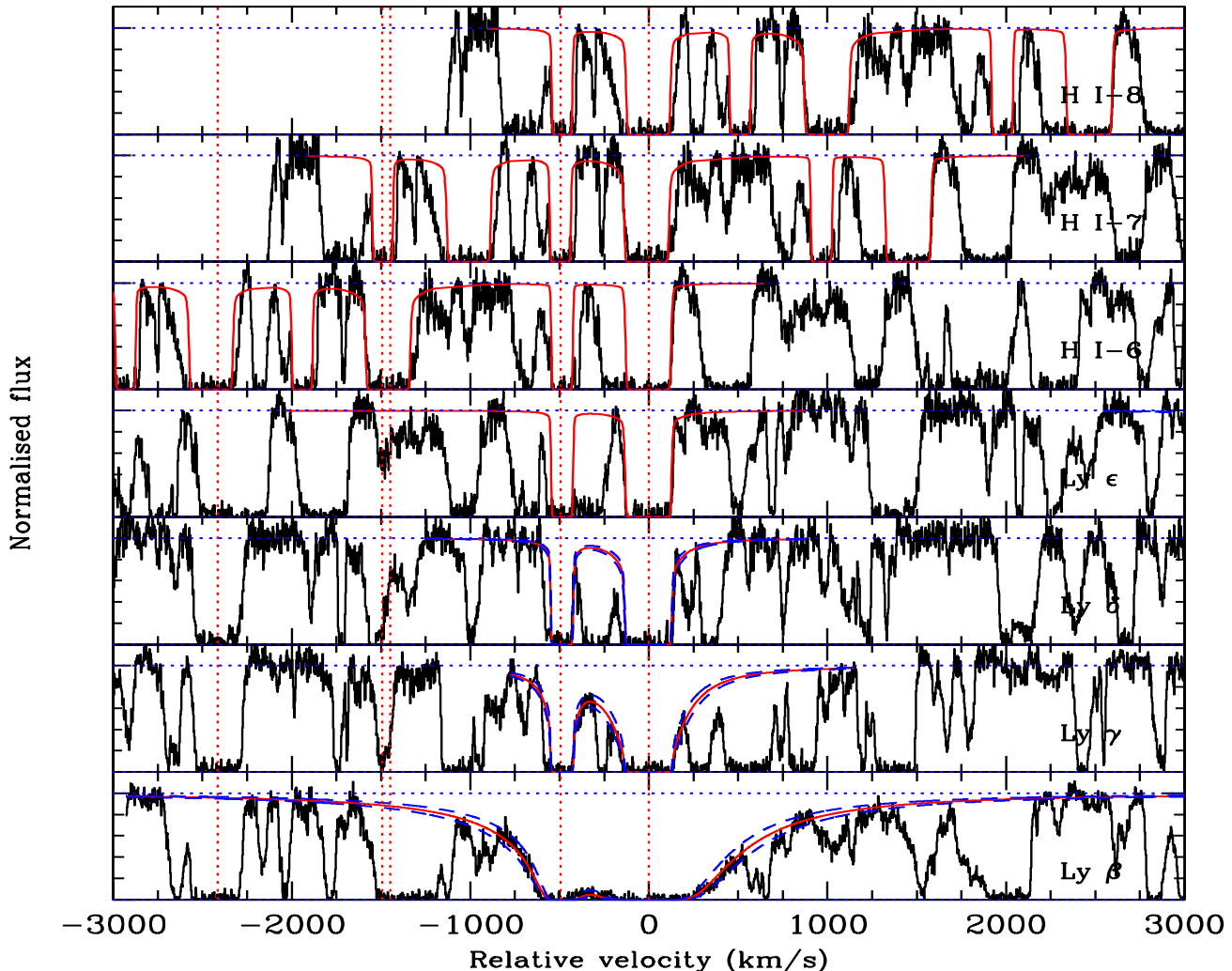


**Figure 2.** Fit to the Lyman series lines of the  $z_{\text{abs}} = 3.17448$  ( $v = 0 \text{ km s}^{-1}$ ) and  $3.16768$  ( $v = -488 \text{ km s}^{-1}$ ) DLA systems. There is a strong Lyman limit system at  $z_{\text{abs}} = 3.1408$  ( $v = -2420 \text{ km s}^{-1}$ ). Some of the Lyman series absorption lines of the  $z_{\text{abs}} = 3.17448$  and  $3.1408$  system happen to be blended. The vertical dashed lines at  $v \sim -1500 \text{ km s}^{-1}$  mark the locations of a C IV system along this line of sight (see also Fig. 5).

source is represented by a single component with flux density  $83 \text{ mJy}$  and a deconvolved size of  $0.75'' \times 0.12''$ . It is compact as well in our GMRT 610-MHz image with similar resolution with a flux density of  $\sim 102 \text{ mJy}$ . The image of highest resolution for this source is from the JVAS/CLASS survey. In this VLA A-array 8 GHz image of resolution  $0.26'' \times 0.22''$  the source is still compact with a flux density of  $25.8 \text{ mJy}$ . In the GB6 catalog at 5 GHz this radio source has a flux density of  $29 \text{ mJy}$ , very similar to the CLASS/JVAS 8 GHz image. Therefore, from the arcsecond and sub-arcsecond scale images available, the source appears to be core dominated with an indication of the low-frequency turnover. We have no reason to believe the covering factor is not close to unity.

The spin temperature measured here is in between the expected kinetic temperatures of cold ( $\leq 300 \text{ K}$ ) and warm ( $5000\text{--}8000 \text{ K}$ ) neutral media (Wolfire et al. 2003). Thus, what we measure can be interpreted as the harmonic mean

temperature of the multiphase medium along the line of sight. Interestingly the spin temperature we measure here is consistent with the mean spin temperature measured in very low redshift QSO-galaxy pairs (Carilli & van Gorkom 1992).

## 4.2 Molecular Hydrogen

Weak Lyman and Werner band  $\text{H}_2$  absorption lines from different rotational levels of the vibrational ground state are detected in system-1. The spectrum at the positions of different  $\text{H}_2$  absorption lines together with single component Voigt profile fits to these lines are shown in Fig. 3. All the lines except  $\text{H}_2\text{W}_3\text{R}_1$  and  $\text{H}_2\text{L}_5\text{R}_0$  were used during the fits for which  $z$  and  $b$  were assumed to be the same for all  $J$  levels. The reduced  $\chi^2$  for the best fit is 1.4. Corresponding parameters are summarised in Table 1.

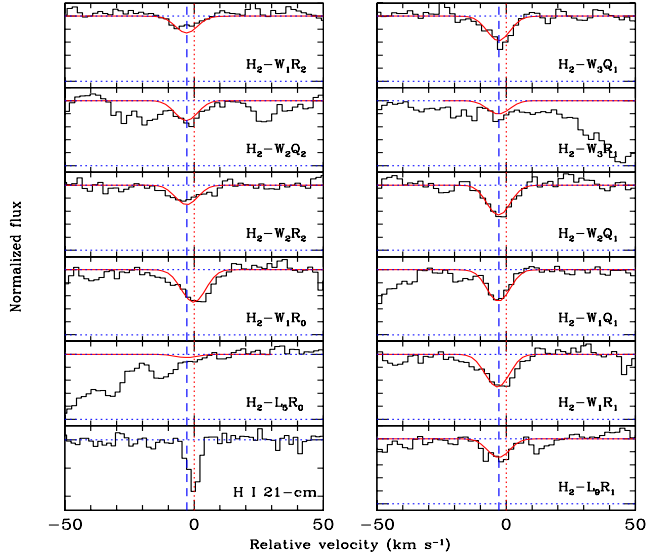


**Figure 3.** Voigt profile fits to  $H_2$  Lyman and Werner band absorption lines. The vertical dotted and dashed lines mark the locations of the 21-cm and  $H_2$  absorption lines, respectively. The apparent shift between the two lines is  $\sim 2.7 \text{ km s}^{-1}$ . The zero of the velocity scale is defined with respect to the redshift of the  $H_2$  lines,  $z_{\text{abs}} = 3.174441$ .

**Table 1.** Results of single component fits to  $H_2$  lines in system-1

Level	$z$	$b$ ( $\text{km s}^{-1}$ )	$\log N(H_2, J)$ ( $\text{cm}^{-2}$ )
J=0	3.174441(5)	$4.6 \pm 0.4$	$12.88 \pm 0.16$
J=1	....	....	$13.85 \pm 0.04$
J=2	....	....	$13.65 \pm 0.04$
J=3	....	....	$\leq 13.47$

For  $J = 0$ , most of the lines are blended in the Lyman- $\alpha$  forest and the quoted column density is constrained by the strength of the  $H_2 W_1 R_0$  absorption. The large error is due to the fact that this line is blended with  $H_2 W_1 R_1$ . Similarly, in the case of  $J = 3$ , most of the strongest transitions are blended with other lines in the Lyman- $\alpha$  forest. We use the expected position of the  $H_2 W_3 R_3$  line to derive an upper limit on  $N(H_2, J=3)$ .

From the total  $H_2$  column density and the above measured  $N(H I)$  we derive the molecular fraction in the cloud:  $f_{H_2} \simeq 2N(H_2)/N(H I) = 1.0 \times 10^{-7}$  which is the lowest value measured in a DLA (see Table 1 of Noterdaeme et al. (2008a)). The low  $f_{H_2}$  could be the result of either or both low dust content and excess UV flux from the QSO.

The  $J = 1$  excitation temperature is usually used as an estimator of the kinetic temperature. However, it is known that this estimator is robust only when the total  $H_2$  column density is in excess of  $10^{16} \text{ cm}^{-2}$  (Roy et al. 2006), which is far from being the case here. Indeed, the column density ratio  $N(H_2, J=1)/N(H_2, J=0)$  measured here is higher than, or close to 9, the maximum value allowed by the Boltzmann distribution. Note that this has already been observed in the

**Table 2.** Results of Voigt profile fits to the metal lines in system-1 at  $z_{\text{abs}} = 3.17447$

Species	$z$	$\log N$ ( $\text{cm}^{-2}$ )	$b$ ( $\text{km s}^{-1}$ )	$[X/S]^a$
N I	3.174025	$13.78 \pm 0.03$	$11.3 \pm 0.6$	$-0.95 \pm 0.05$
Si II	....	$14.60 \pm 0.09$	....	$+0.26 \pm 0.10$
S II	....	$13.98 \pm 0.04$	....	....
Fe II	....	$13.90 \pm 0.02$	....	$-0.38 \pm 0.09$
C II*	3.174387	$13.34 \pm 0.04$	$8.3 \pm 0.4$	....
C I	....	$\leq 12.30$	....	....
N I	....	$14.68 \pm 0.02$	....	$-0.87 \pm 0.03$
O I	....	$16.25 \pm 0.10$	....	$-0.08 \pm 0.10$
Mg II	....	$15.13 \pm 0.06$	....	$-0.05 \pm 0.06$
Si II	....	$15.17 \pm 0.04$	....	$+0.00 \pm 0.04$
S II	....	$14.80 \pm 0.02$	....	....
Ar I	....	$13.62 \pm 0.06$	....	$-0.38 \pm 0.10$
Cr II	....	$13.00 \pm 0.17$	....	$-0.29 \pm 0.17$
Fe II	....	$14.53 \pm 0.03$	....	$-0.57 \pm 0.08$
Ni II	....	$13.41 \pm 0.04$	....	$-0.44 \pm 0.04$
Zn II	....	$12.17 \pm 0.25$	....	$-0.10 \pm 0.25$
C II*	3.174473	$13.27 \pm 0.07$	$2.5 \pm 0.6$	....
C I	....	$\leq 12.30$	....	....
N I	....	$14.12 \pm 0.15$	....	$-1.38 \pm 0.26$
O I	....	$16.60 \pm 0.13$	....	$+0.32 \pm 0.16$
Mg II	....	$15.03 \pm 0.06$	....	$-0.10 \pm 0.22$
Si II	....	$15.11 \pm 0.11$	....	$+0.00 \pm 0.24$
S II	....	$14.75 \pm 0.21$	....	....
Ar I	....	$13.70 \pm 0.08$	....	$-0.25 \pm 0.23$
Cr II	....	$12.89 \pm 0.22$	....	$-0.35 \pm 0.30$
Fe II	....	$14.61 \pm 0.07$	....	$-0.44 \pm 0.23$
Ni II	....	$13.26 \pm 0.05$	....	$-0.54 \pm 0.22$
Zn II	....	$\leq 12.30$	....	....

<sup>a</sup> Solar photospheric abundances are from Asplund et al. (2009).

low- $N(H_2)$   $z_{\text{abs}} = 3.0248$  system toward Q 0347–383 (see Ledoux et al. (2003), Srianand et al. (2005)).

From Fig. 3 it is apparent that, while the 21-cm absorption is well within the velocity range of the  $H_2$  absorption, the centroid of the  $H_2$  absorption lines is shifted by  $2.7 \pm 1.0 \text{ km s}^{-1}$  with respect to the centroid of the 21-cm absorption line for the single component fit. If we use the two component gaussian fit to the 21-cm line then the redshift of the weak 21-cm absorption component is consistent with that of the  $H_2$  absorptions within measurement uncertainties. The basic observation remains, however, that the optical depth ratio between  $H_2$  and 21-cm absorption varies inside the absorbing cloud.

### 4.3 Heavy element abundances and dust content

We performed simultaneous Voigt profile fits to metal absorption line features from neutral and singly ionized species (see Fig. 4). The best fit is obtained with three components at  $z_{\text{abs}} = 3.174025$ ,  $3.174387$  and  $3.174473$ . First two components have relative velocities compared to the third one of  $\Delta v = -32$  and  $-6 \text{ km s}^{-1}$  respectively. Fit parameters are summarized in Table 2, where the last column gives relative abundances with respect to Sulfur in each component without applying any ionization correction.

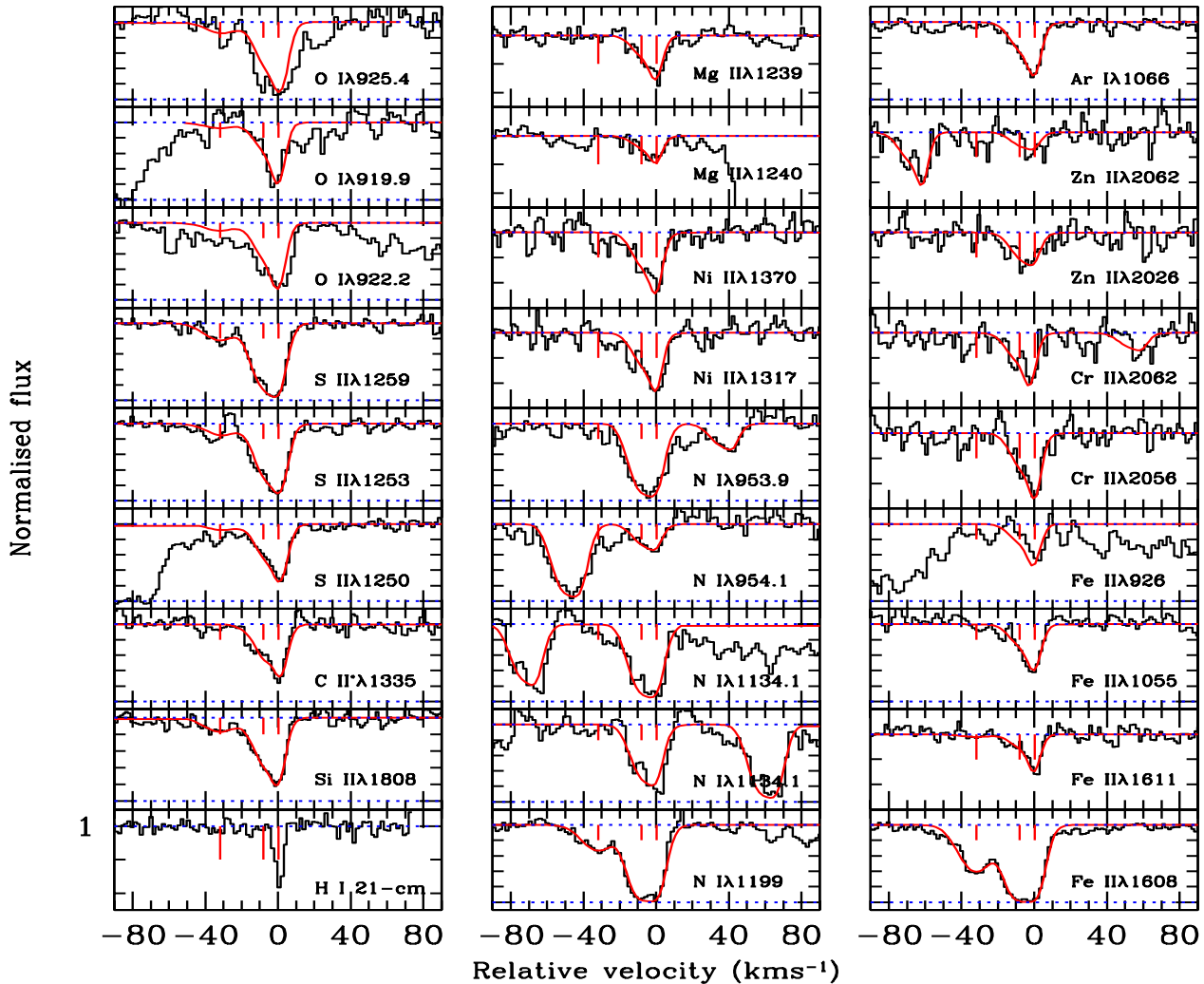


**Figure 4.** Voigt profile fits to a selected set of metal absorption lines from system-1 at  $z_{\text{abs}} = 3.17447$ . Vertical tick marks indicate the locations of the three velocity components.

In Fig. 4, we also plot the 21-cm absorption profile for comparison. It is clear from this figure that the strongest and narrow metal line component at  $z_{\text{abs}} = 3.174473(6)$  is well aligned with the 21-cm absorption. It is also clear from Table 2 that there is no strong component to component variation in the depletion pattern among the three components which is consistent with what is observed in typical DLAs (Rodríguez et al. 2006).

Based on the robust column densities of Si II, S II and Fe II we find the main component at  $z_{\text{abs}} = 3.174473$  to contain 40 to 45% of the total column density detected in this DLA. As there is no reason to believe the metallicity in this component is less than in the other two components, it is most likely that only 40 to 45% of the total H I column density is associated with this component. In that case we derive  $T_s \sim 270_{-72}^{+100}$  K for this component. This brings the spin temperature very close to what is expected in a cold neutral medium (CNM). It is also interesting to note that

there is no indication of a distinct narrow metal component coinciding with the H<sub>2</sub> position supporting the fact that the cloud is not strictly homogeneous and that the H<sub>2</sub> and 21-cm narrow components are consequences of physical conditions in the cloud changing on small scale.

Adding column densities from the three components, we derive the average metallicities in the DLA given in Table 3. The  $\alpha$  element metallicity is  $[\text{Si}/\text{H}] \sim [\text{S}/\text{H}] = -1.45 \pm 0.22$ . The oxygen abundance measured from the unblended lines matches well (i.e.  $[\text{O}/\text{S}] = 0.05 \pm 0.29$ ) with that of other  $\alpha$  elements although the errors are large.

The nitrogen abundance measurement is robust and we find  $[\text{N}/\alpha] \sim -1.0$ . This is consistent with what is seen in low metallicity DLAs (see Petitjean et al. 2008; Pettini et al. 2008b) and very different of what is usually measured in gas associated with QSOs (Petitjean et al. 1994; Hamann & Ferland 1993).

From Table 3, it can be seen that Ar seems slightly

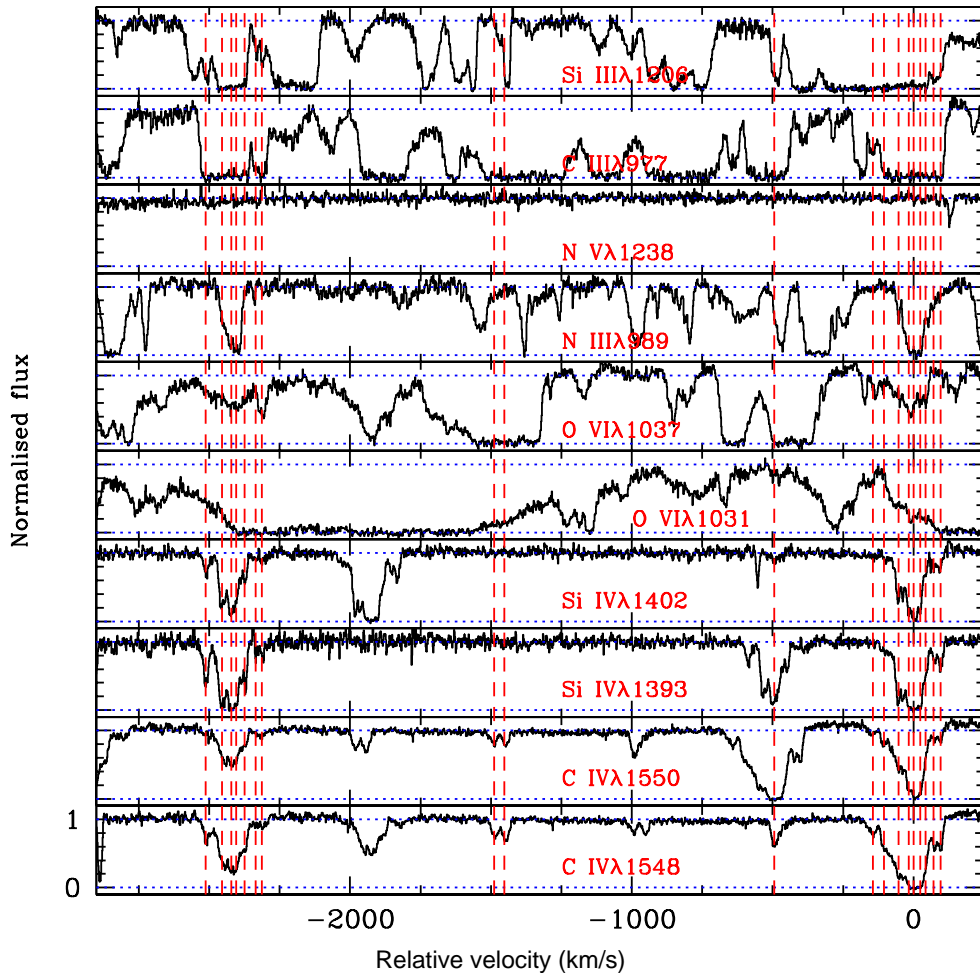


**Figure 5.** Velocity plot of metal absorption lines of highly ionized species. The velocity scale is defined with respect to the DLA at  $z_{\text{abs}} = 3.17447$ . Dashed vertical lines mark the locations of C IV components. The system at  $v \sim -500 \text{ km s}^{-1}$  corresponds to the DLA at  $z_{\text{abs}} = 3.16768$ . The vertical dashed lines around  $v \sim -2420 \text{ km s}^{-1}$  are the C IV components of a LLS at  $z_{\text{abs}} = 3.1408$ . The C IV components marked at  $v \sim -1500 \text{ km s}^{-1}$  are from an intervening high column density Lyman- $\alpha$  system.

( $\sim 0.4$  dex) underabundant compared to other  $\alpha$  elements. Such deficiency has been noted already in the Galactic ISM and in high redshift DLAs (Vladilo et al. 2003; Ledoux et al. 2006). This has been attributed to the large photoionization cross-section of Ar I above 15 eV (Sofia & Jenkins 1998). We can use this argument to constrain the ionization parameter in the absorbing gas (see below). Since the [Ar/Si] ratio is about the same in the individual components (see Table 2), we can infer that the effect of ionization is nearly identical in the different components.

The Zn II transitions are weak and the corresponding column densities are difficult to measure. The [Zn/Cr] metallicity ratio is close to solar while Fe, Cr and Ni are slightly underabundant compared to S and Si. If we attribute this to dust depletion, then we can infer that a maximum of 60% of Fe has gone into dust. In turn, the very low abundance of  $\text{H}_2$  may indicate that the gas is dust free with a slight enhancement of  $\alpha$  element abundances. The chemical properties of this system are very similar to the  $z_{\text{abs}} = 2.402$  DLA

towards HE 0027–1836, that also shows low metallicity and low molecular fraction (Noterdaeme et al. 2007).

From Fig. 5 it can be seen that C IV and Si IV absorption lines are very strong in this DLA. N V is absent even though the absorption redshift is close to the QSO emission redshift. The absorption lines are seen at the expected positions of C III, N III, Si III and O VI transitions. However, as these transitions are redshifted within the Lyman- $\alpha$  forest it is very difficult to confirm them. This indicates however that a wide range of ionization states coexist in this system. Absence of N V and the possible presence of O VI is consistent with what is typically seen in DLAs (see Fox et al. 2007).

#### 4.4 Physical conditions in the absorbing gas

Here, we discuss the physical conditions in the gas associated with system-1 using simple photoionization models using CLOUDY (Ferland et al. 1998). The aim is not to de-

**Table 3.** Average metallicities in system-1 at  $z_{\text{abs}} = 3.17447$ 

Species	$\log N$ ( $\text{cm}^{-2}$ )	$\log Z/Z_{\odot}^a$
H I	$21.36 \pm 0.10$	....
C I	$\leq 12.60$	....
C II*	$13.61 \pm 0.08$	....
N I	$14.83 \pm 0.06$	$-2.44 \pm 0.12$
O I	$16.76 \pm 0.16$	$-1.40 \pm 0.19$
Mg II	$15.59 \pm 0.08$	$-1.35 \pm 0.13$
Si II	$15.50 \pm 0.15$	$-1.42 \pm 0.18$
S II	$15.11 \pm 0.20$	$-1.45 \pm 0.22$
Ar I	$13.96 \pm 0.10$	$-1.80 \pm 0.14$
Cr II	$13.25 \pm 0.28$	$-1.79 \pm 0.30$
Fe II	$14.91 \pm 0.08$	$-1.95 \pm 0.13$
Ni II	$13.64 \pm 0.15$	$-1.97 \pm 0.18$
Zn II	$12.26 \pm 0.26$	$-1.77 \pm 0.28$

<sup>a</sup> solar photospheric abundances are from Asplund et al. (2009).

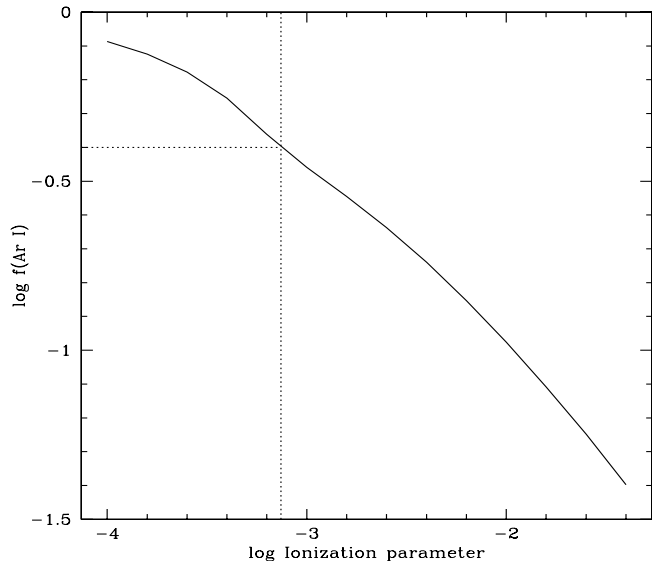
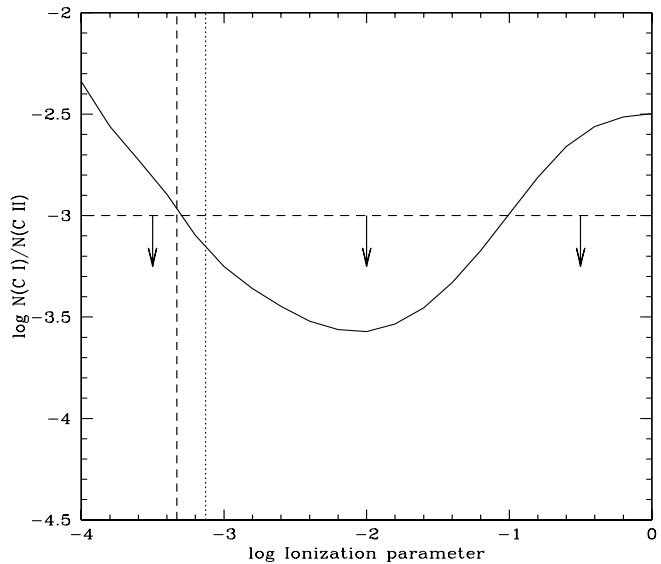
scribe in detail the system but rather to estimate the ionization parameter using  $N(\text{Ar I})$ , the particle density using  $N(\text{C II}^*)$  and to constrain the distance of the absorbing gas from the QSO.

We assume the absorbing cloud to be a plane parallel slab of constant density, the ionizing radiation to be that of a typical QSO (i.e Mathews & Ferland (1987)),  $\log N(\text{H I}) = 21.3$  and  $Z = -1.4 Z_{\odot}$ . The observed dust to metal ratio in the system is  $\sim 60\%$  of the Galactic value. Together with the measured metallicity we find the dust to gas ratio to be roughly 2% of what is measured in the cold phase of the neutral galactic ISM (Welty et al. 1999). We use this value in our model and assume the dust composition to be similar to that in the galactic ISM.

#### 4.4.1 Constraints on the ionization parameter

In Fig. 6 we plot the Ar I/Ar ratio as a function of the ionization parameter,  $U$ . Assuming solar  $[\text{Ar}/\text{S}]$  (and/or  $[\text{Ar}/\text{Si}]$ ) abundance ratio, we derive from the  $N(\text{Ar I})/N(\text{S II})$  (and/or  $N(\text{Ar I})/N(\text{Si II})$ ) ratio given in Table 3 that the  $\text{Ar}^0/\text{Ar}$  ratio is larger than 0.4. From Fig. 6 we conclude  $U < 10^{-3.1}$ . Note that as the average  $\text{Ar}^0/\text{Ar}$  ratios are similar in different components, this result will hold for individual components as well.

In principle we can derive a lower limit on the ionization parameter from the upper limit on  $N(\text{C I})$ . As the C II absorption lines available in our spectrum are heavily saturated we have to assume a value of the  $[\text{C}/\text{Si}]$  abundance ratio. From Fig. 3 of Petitjean et al. (2008) we note that Si and O abundances follow each other very well over a wide range of metallicities. However, carbon can be underabundant (by  $\sim 0.5$  dex) compared to oxygen for  $[\text{O}/\text{H}] \sim -1.4$  as observed in this system. Using  $[\text{C}/\text{Si}] = -0.5$ , we derive  $\log N(\text{C II}) = 15.96 \pm 0.15$  (i.e  $\log N(\text{Si II}) + 8.52 - 7.56 - 0.50$ ). This, together with the  $3\sigma$  upper limit on  $N(\text{C I})$ , gives  $N(\text{C I})/N(\text{C II}) \leq 10^{-3}$ . Fig. 7 gives the  $N(\text{C I})/N(\text{C II})$  ratio through the cloud model versus ionization parameter. The above condition implies  $\log U > -3.3$ . We therefore find  $-3.3 \leq \log U \leq -3.1$  and we will take  $\log U = -3.2$  as a typical value for further discussions.

**Figure 6.** Fraction of neutral Ar as a function of the ionization parameter.**Figure 7.** The predicted  $N(\text{C I})/N(\text{C II})$  ratio as a function of ionization parameter.

#### 4.4.2 Fine-structure lines and particle density

The only fine-structure absorption line seen in this system is  $\text{C II}^* \lambda 1335$ . Using the same assumptions as above, we can derive  $\log N(\text{C II}^*)/N(\text{C II}) = -2.45 \pm 0.16$  from the observations. Interestingly this is consistent with what is expected in the case of CNM gas with low metallicity (See fig. 15 of Srianand et al. 2005).

In the absence of C I and associated fine-structure lines it is not easy to derive  $n_{\text{H}}$  as the  $\text{C II}^*$  column density depends on the ionization fraction of the gas and the kinetic temperature (see, for example, the discussion in sec-



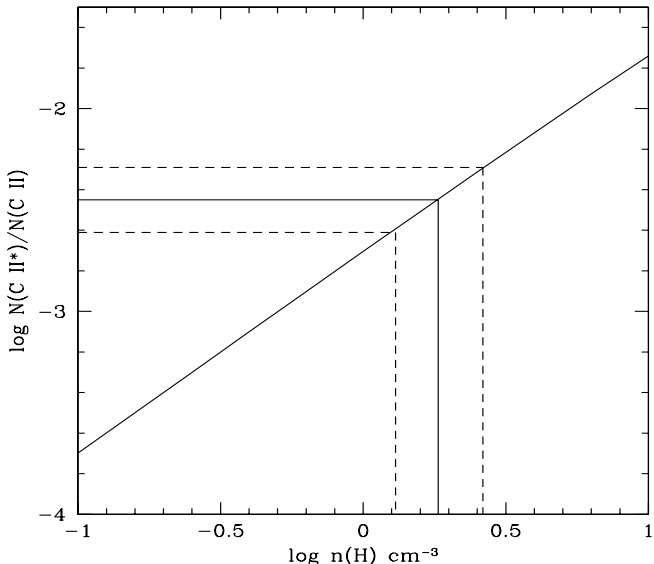


**Figure 8.** The slanted solid line gives the  $\log N(\text{C II}^*)/N(\text{C II})$  ratio as a function hydrogen density. The observed mean and  $1\sigma$  ranges for  $N(\text{C II}^*)/N(\text{C II})$  are given by horizontal solid line and dashed lines, respectively. The intersections of these lines with the model curve give the allowed density range.

tion 6 of Srianand et al. 2005). Therefore, to interpret the  $N(\text{C II}^*)/N(\text{C II})$  ratio, we will rely on a photoionization model. We run a grid of Cloudy models keeping constant the ionization parameter,  $\log U = -3.2$ , as constrained above,  $T = 600$  K, as derived from the 21-cm spin temperature measurements, and varying the particle density in the range 0.1 to  $10 \text{ cm}^{-3}$ .

The model predictions on  $N(\text{C II}^*)/N(\text{C II})$  are given in Fig. 8 as a function of the particle density. We derive  $1.3 \leq n_{\text{H}} (\text{cm}^{-3}) \leq 2.6$ . Thus a value of  $2 \text{ cm}^{-3}$  is representative of the particle density in this system when we assume  $\log U = -3.3$ . Cloudy also predicts the column densities of the O I and Si II fine-structure lines and the predicted values are consistent with the non-detections of these species in our data.

As an aside, we notice that while most of the constraints based on atomic species are satisfied by the model presented here, the latter predicts high values of  $N(\text{H}_2)$  (remember we use a dust to gas ratio equal to 2% of the Galactic ISM value). However, models with very low dust content (i.e dust to gas ratio  $\leq 0.1\%$  of the Galactic ISM) predict an amount of  $\text{H}_2$  consistent with our observations. Thus it may be possible that the observed lower abundance of Fe co-production elements does not reflect dust depletion but real nucleosynthetic underabundance.

#### 4.4.3 Constraints on the distance to the quasar

From the estimates of the ionization parameter and particle density, we can constrain the distance of the absorbing cloud from the QSO. The Lyman limit of the absorber in our observed frame is at  $\lambda \sim 3807 \text{ \AA}$ . From the flux calibrated SDSS spectrum we find  $f_{\nu} = 70 \mu\text{Jy}$  at this wavelength. For a flat cosmological model with  $\Omega_{\Lambda} = 0.73$ ,  $\Omega_{\text{m}} = 0.27$  and

$h = 0.7$  we find the luminosity distance of the QSO to be  $2.8 \times 10^{28} \text{ cm}$ . This gives the luminosity at the Lyman limit,  $L_{\nu}(\text{LLS}) = 1.7 \times 10^{30} \text{ ergs s}^{-1} \text{ Hz}^{-1}$  and the rate of hydrogen ionizing photons,  $Q(\text{H}) = 2.6 \times 10^{56} \text{ photons s}^{-1}$ , when we assume a flat spectrum. The ionization parameter is usually defined as,

$$U = \frac{Q(\text{H})}{4\pi r_c^2 \text{cm}}. \quad (2)$$

Here,  $r_c$  is the distance of the cloud from the QSO and  $n$  is the particle density in the absorbing gas. Using  $n \sim 2 \text{ cm}^{-3}$  and  $U = 5 \times 10^{-4}$  we get  $r_c \sim 270 \text{ kpc}$ . This also means that, if in situ star formation controls the ionization state of the gas then the DLA has to be at a distance much larger than 270 kpc from the QSO.

This clearly shows that the absorbing gas is not associated with the QSO host galaxy. The gas could be associated with a galaxy in the group or cluster in which the QSO resides. In this sense this system is very similar to that of the  $z_{\text{abs}} = 2.8112$  DLA towards PKS 0528–250 (Srianand & Petitjean 1998; Moller & Warren 1998).

## 4.5 Constraining fundamental constants

As the energy of the hyperfine H I 21-cm transition is proportional to the combination of three fundamental constants,  $x = \alpha^2 G_{\text{p}}/\mu$ , high resolution optical and 21-cm spectra can be used together to probe the combined cosmological variation of these constants (Tubbs & Wolfe 1980). For the  $z_{\text{abs}} = 1.7764$  system towards Q 1337+170, Cowie & Songaila (1995) have obtained  $\Delta x/x = (z_{\text{UV}} - z_{21})/(1 + z_{21}) = (0.7 \pm 1.1) \times 10^{-5}$ . Here,  $z_{\text{UV}}$  and  $z_{21}$  are the redshifts of the UV lines and 21-cm absorption, respectively. Tzanavaris et al. (2005) obtained  $\Delta x/x = (0.63 \pm 0.99) \times 10^{-5}$  using this technique and a sample of 8 published systems. Similarly, Kanekar et al. (2006) derived  $\Delta x/x = (-0.15 \pm 0.62) \times 10^{-5}$  at  $z_{\text{abs}} = 2.34786$  towards PKS B0438–438.

The measured wavelengths of H<sub>2</sub> Lyman and Werner band transitions can be used to probe the variation of  $\mu$  (Varshalovich & Levshakov 1993). The presence of H<sub>2</sub> together with 21-cm absorptions can, in principle, allow us to place constraints on  $\alpha$  and  $\mu$  in the same system. In this regard, the system studied here is unique. However, as the H<sub>2</sub> column density is weak, only Werner band absorption lines are seen. Therefore and unfortunately, the range of sensitivity coefficients of the detected lines is too narrow to provide stringent constraints. Using a linear regression analysis, we derive  $\Delta\mu/\mu \leq 4.0 \times 10^{-4}$  and  $\bar{z}_{\text{H}_2} = 3.174442 \pm 0.000014$ . The upper limit on  $\Delta\mu/\mu$  measured here is roughly an order of magnitude larger than the typical estimates based on H<sub>2</sub> lines published till now [see Ivanchik et al. (2005), Reinhold et al. (2006), King et al. (2008) and Thompson et al. (2009)].

As discussed before, the single component fit to the 21-cm absorption gives  $z_{21} = 3.174480 \pm 0.000002$ . The strongest metal line component is seen at  $z_{\text{UV}} = 3.174473 \pm 0.000006$ . From these two redshifts, we derive  $\Delta x/x = -(1.7 \pm 1.5) \times 10^{-6}$ . We find the wavelength calibration accuracy is  $\leq 4 \text{ m\AA}$  during the pipeline data reduction (see also Chand et al. 2006). This translates to an error of  $4 \times 10^{-6}$  (or a velocity uncertainty of  $0.3 \text{ km s}^{-1}$ ) in the redshift measurement at the

mean observed wavelength ( $\sim 4500\text{\AA}$ ) of the lines used to derive  $z_{\text{UV}}$ . If we include this error also then we get  $\Delta x/x = -(1.7 \pm 1.7) \times 10^{-6}$ .

If we assume no variation in  $\alpha$  and  $G_{\text{p}}$  (respectively  $\mu$  and  $G_{\text{p}}$ ) then this limit translates to  $\Delta\mu/\mu = -(1.7 \pm 1.7) \times 10^{-6}$  (respectively  $\Delta\alpha/\alpha = -(0.85 \pm 0.85) \times 10^{-6}$ ). These constraints alone are more stringent than most of the published values in the literature.

However, we like to point out that our UVES spectrum was taken as part of our ongoing survey for molecules in DLAs where ThAr calibration frames were not taken immediately after the science observations. This may induce an additional systematic error of the same order as our measurement errors. In addition, the velocity offset we noticed between  $\text{H}_2$  and 21-cm absorption could reflect inhomogeneities in the gas which could contribute to additional systematic error. This kind of systematics can only be alleviated through randomization using a large and well defined sample that we want to build in the future. Note that the velocity shift could be related to covering factor issues if the radio source shows structures at the milli-arcsec scale. Thus, as for any other system, high resolution VLBA observations are needed to support the analysis towards constraining variations in  $x$ .

## 5 ANALYSIS OF SYSTEM-2 ( $z_{\text{abs}} = 3.16768$ )

Molecular hydrogen and  $\text{C II}^*$  absorption lines are not detected in this DLA with  $\log N(\text{H I}) = 20.41 \pm 0.15$ . The  $2\sigma$  upper limit on the molecular fraction is  $f_{\text{H}_2} < 2 \times 10^{-7}$ . In addition, as our GMRT observations were performed prior to our UVES observations, we did not cover the expected frequency range for the redshifted 21-cm line. However, this system is very interesting as the metal lines from strong resonance transitions are unsaturated and D I absorption can be fitted. This makes it possible for us to understand the chemical evolution and deuterium astration factor in this system which is at an early stage of chemical evolution.

### 5.1 Heavy element abundances and dust

Low ionization metal absorption lines detected in this system together with the best fitted Voigt profiles are shown in Fig. 9. The strongest transitions of C II, Si II and O I are not strongly saturated and can be used to derive column densities. The absorption profiles are well fitted with four components at  $v = -7.7, 0, 12.4$  and  $17.8 \text{ km s}^{-1}$  with respect to  $z_{\text{abs}} = 3.16768$ .

Table 4 summarises the total column densities of neutral and low ionization species and the corresponding metallicities measured in this system assuming no ionization correction. The oxygen metallicity is one of the lowest known among DLAs and sub-DLAs (see Petitjean et al. (2008); Pettini et al. (2008b)). We remind the reader that the low oxygen metallicity cannot be due to ionization effects because O I is known to be coupled tightly with H I through charge exchange reactions. Actually the carbon, silicon, aluminium and iron metallicities estimated from the singly ionized species are consistent with  $[\text{O}/\text{H}]$ .

The system is of low-ionization. We detect the Si III  $\lambda 1206$  line and measure  $\log N(\text{Si III}) = 13.28 \pm 0.06$ , but

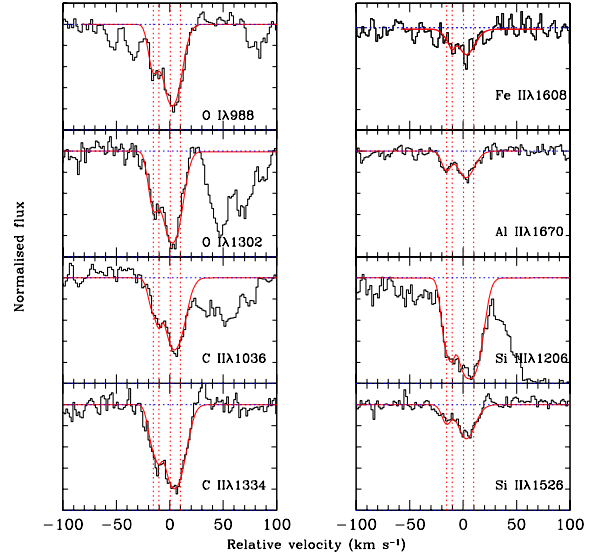


**Figure 9.** Multicomponent Voigt profile fits to absorption features in the  $z_{\text{abs}} = 3.16768$  system. Vertical dotted lines mark the locations of individual components.

**Table 4.** Total column density and average metallicity in the  $z_{\text{abs}} = 3.16768$  DLA

Species	$\log N$ ( $\text{cm}^{-2}$ )	$\log Z/Z_{\odot}^a$
H I	$20.41 \pm 0.15$	....
N I	$\leq 12.80$	$\leq -3.53$
O I	$14.43 \pm 0.09$	$-2.64 \pm 0.17$
C II	$13.98 \pm 0.06$	$-2.82 \pm 0.16$
Si II	$13.24 \pm 0.05$	$-2.68 \pm 0.16$
Si III	$13.28 \pm 0.06$	
Al II	$12.00 \pm 0.05$	$-2.78 \pm 0.16$
Fe II	$13.14 \pm 0.26$	$-2.72 \pm 0.30$

<sup>a</sup> solar photospheric abundances are from Asplund et al. (2009)

the Si IV absorption is very weak (see Fig. 5). Therefore, in any case the silicon abundance is  $[\text{Si}/\text{H}] < -2.38 \pm 0.13$ .

The spectrum covers the expected position of C III  $\lambda 987$  but this line is blended with intervening Lyman- $\alpha$  absorptions (see Fig. 5). C IV absorption is also weak. The column density of C II implies  $[\text{C}/\text{O}] \geq -0.18 \pm 0.18$ . This value contradicts the result of standard galactic chemical evolution models (see Akerman et al. (2004)) expecting the carbon metallicity to be much smaller than the oxygen metallicity (i.e  $[\text{C}/\text{O}] < -0.5$ ) for  $[\text{O}/\text{H}] < -2$ . However, our result is consistent with results by Pettini et al. (2008b) and supports the suggestion by Akerman et al. (2004) that carbon and oxygen may be produced in near-solar proportions in the earliest stages of galactic chemical evolution. Chemical evolution models with Population III stars (Chieffi & Limongi (2002)) or with fast rotating stars (Chiappini et al. (2006)) produce near solar  $[\text{C}/\text{O}]$  at low metallicities.

The spectrum does not show detectable absorption lines of N I. Hence, we only derive an upper limit for  $N(\text{N I})$ .

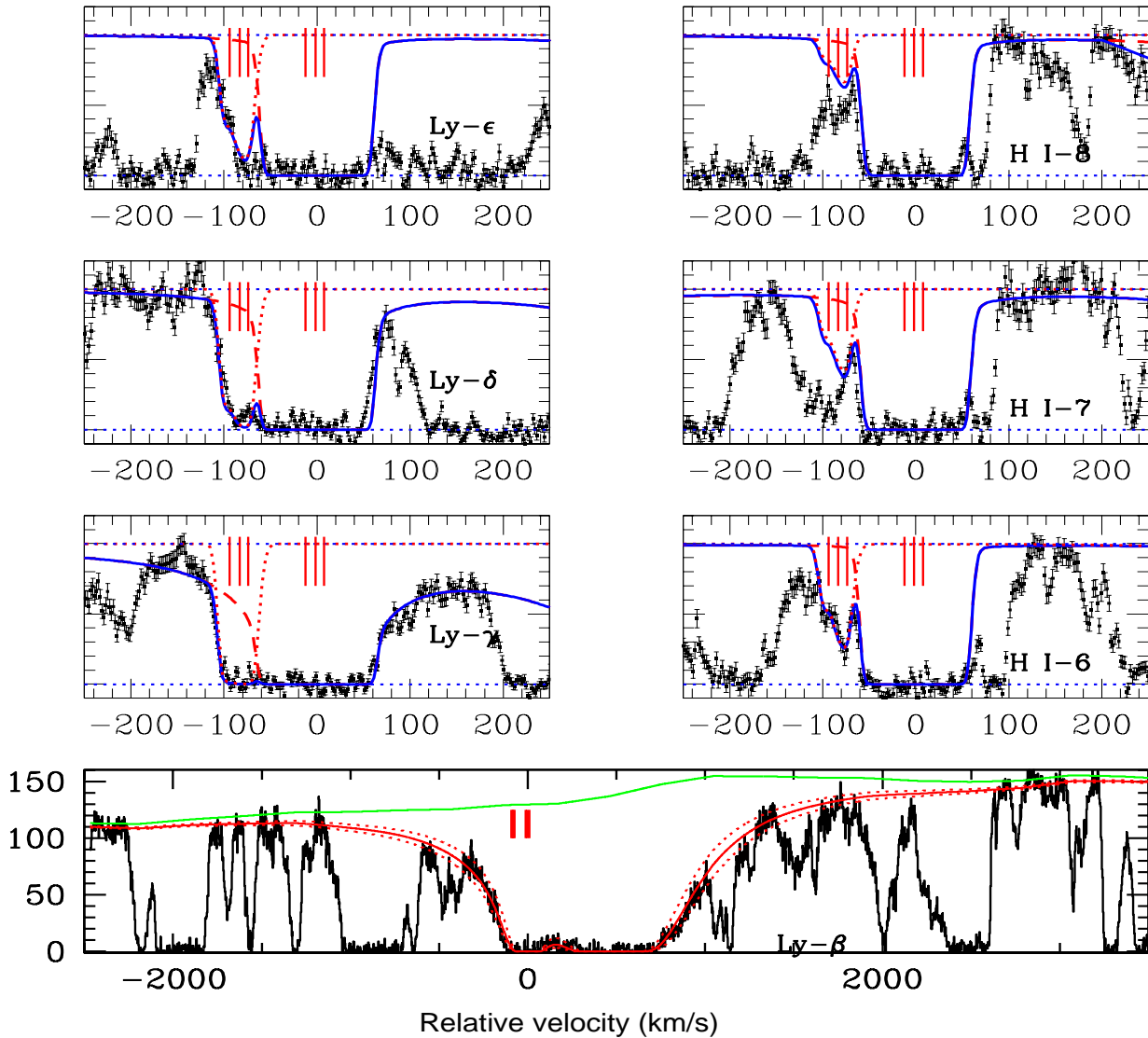


**Figure 10.** Voigt profile fits to the Lyman series lines in the  $z_{\text{abs}} = 3.1678$  system. Ticks around  $v \sim 0 \text{ km s}^{-1}$  mark the locations of the metal line components. The Voigt profile parameters giving good fits to the damping wings of Lyman- $\beta$ , the red wings of Lyman- $\gamma$  and  $\delta$  and the blue wings of Lyman-6, Lyman-7 and Lyman-8 transitions (profiles with long dashed lines) do not explain the excess absorption at the expected positions of the D I absorption lines (ticks around  $v = -82 \text{ km s}^{-1}$ ). Fits to D I absorption lines are shown with dashed profiles.

The expected wavelength range for N II  $\lambda 1083$  is affected by intervening Lyman- $\alpha$  absorption from the IGM. Using N I/O I we derive  $[\text{N}/\text{O}] \leq -0.89$ . This is not stringent enough to draw conclusions regarding the contribution to the nitrogen metallicity from primary and secondary productions.

Based on the  $[\text{Fe}/\alpha]$  abundance ratio we can conclude that there is no dust depletion in the gas. The absence of H<sub>2</sub> absorption could very well be attributed to the lack of dust in the system. The lack of  $\alpha$  element enhancement also means that the star formation activity is not recent. In addition, this also undermines the contribution of Population III stars to overall enrichment.

## 5.2 Constraint on the D/H ratio

While fitting the Lyman series absorption lines, we find a clear excess absorption in the blue wing of all the available Lyman transitions (see Fig. 10). The total H I column density is well constrained by the damping wings of Lyman- $\beta$  and Lyman- $\gamma$ . The uncertainty in its measurement comes from the error propagated through the Voigt profile fits to the Lyman- $\beta$  absorption of System-1 and from continuum placement. The lower panel of Fig. 10 also shows a typical continuum used near the wavelength range covered by Lyman- $\beta$  line. This was determined using the SDSS composite QSO spectrum (Vanden Berk et al. 2001) with appropriate scaling to fit the line free regions. We constrain

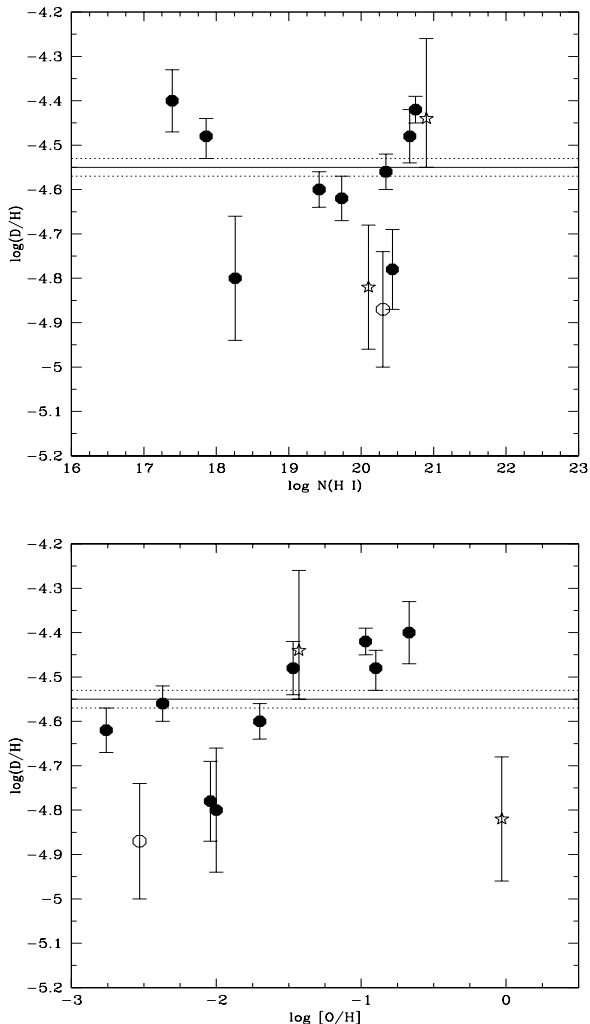


**Figure 11.** *Top panel:* D/H values measured in absorption systems as a function of  $N(H\ I)$ . *Bottom panel:* D/H as a function of metallicity. In both panels the open circle is the measurement presented in this paper. Filled circles are earlier measurements based on  $N(D\ I)/N(H\ I)$  lines from the literature (as summarised in Ivanchik et al. 2010). Stars are the measurements based on HD/2H<sub>2</sub> in two DLAs presented in Noterdaeme et al. (2008b) and Ivanchik et al. (2010).

the velocity dispersion by using the red wings of Lyman- $\gamma$  and  $\delta$  and using the blue wings of Lyman-6, Lyman-7 and Lyman-8. We notice that the resulting best fitting Voigt profiles (dotted profiles in Fig. 10) under-predict the blue wing absorption at  $\sim -82\text{ km s}^{-1}$  for Lyman- $\gamma$ ,  $\delta$  and  $\epsilon$ . Consistent absorption dips are present at similar velocity in the blue sides of higher Lyman series lines. We do not find any metal line absorption at this velocity (see Fig. 9). It is also clear from Fig. 2 that the excess can not be explained by blending with Lyman series lines from the other two strong H I absorption systems seen in the immediate vicinity. Thus it is most likely that the excess absorption in the blue wings of H I lines is due to D I.

We simultaneously fit the D I Lyman series lines with three components at the redshifts of the three strongest O I components that contain  $\sim 96\%$  of the O I column

density. We varied  $N$  and  $b$  for the D I lines to get the best fit. It is to be noted that D I-6 line is unsaturated and the total  $N(D\ I)$  measurement is insensitive to the exact component structure. The results of the Voigt profile fits are shown in Fig. 10. The best fit model gives  $N(D\ I) = (3.0 \pm 0.2) \times 10^{15}\text{ cm}^{-2}$  leading to  $\log(D/H) = \log(D\ I/H\ I) = -4.93 \pm 0.15$ . This is a factor of 2 lower than the primordial value,  $\log[D/H]_p = -4.59 \pm 0.02$ , derived from five-year data of the Wilkinson Microwave Anisotropy Probe (WMAP)(Komatsu et al. 2009).

For the metallicity estimated in this system, it is believed that  $[D/H]$  will be close to  $[D/H]_p$ . However, the present system seems to have lost an appreciable fraction of deuterium during its evolution. In Fig. 11 we plot D/H measured in this system together with those from the literature as a function of  $N(H\ I)$  and  $[O/H]$ . The literature data includes the systems listed by Pettini et al. (2008a) together with the measurement by Crighton et al. (2004) in a Lyman limit absorption system at  $z = 3.256$  towards PKS 1937-1009 and the measurement in the  $z_{\text{abs}} = 3.02$  DLA towards 0347-3819 (Levshakov et al. 2002). For this system, we use the  $[O/H]$  measurement given in Petitjean et al. (2008). We also plot the D/H measurements based on the HD/H<sub>2</sub> ratio by Noterdaeme et al. (2008b) and Ivanchik et al. (2010). In both panels of Fig. 11 the horizontal lines give the weighted mean and  $1\sigma$  range reported by Pettini et al. (2008a) using their sample of 7 measurements.

The latter authors identify two outliers, the  $z_{\text{abs}} = 2.07623$  DLA towards Q 2206-199 (Pettini & Bowen 2001) and the  $z_{\text{abs}} = 2.50357$  partial Lyman limit system towards Q 1009+299 (Burles & Tytler 1998), that may be responsible for the scatter in their sample. Interestingly, the value measured here is consistent with  $\log(D/H) = -4.78 \pm 0.09$  measured in the  $z_{\text{abs}} = 2.07623$  metal poor DLA towards Q 2206-199. Therefore, addition of our measurement to the existing sample increases the scatter (see Fig. 11). It is also interesting to note that a trend seems to exist for higher D/H values at higher oxygen metallicity which may be difficult to understand.

As the absorption lines of H I and D I fall inside the Lyman- $\alpha$  forest one can always question the accuracy of column density measurements. As we use damping wings, the  $N(H\ I)$  measurement is robust as is our lower limit on the astration factor. Indeed, if the deuterium absorption features are due to intervening Lyman- $\alpha$  clouds, the astration factor must be even larger.

There are recent indications that infalling gas may cause astration factor to be different from that predicted by chemical evolution closed box models. Noterdaeme et al. (2008b) measured a relatively low astration factor of deuterium coupled with a high metal enrichment in the  $z_{\text{abs}} = 2.418$  DLA towards Q 1439+1117. Ivanchik et al. (2010) have reported a  $[D/H]$  value close to  $[D/H]_p$  for the  $z_{\text{abs}} = 2.338$  DLA towards Q 1232+0815 based on H<sub>2</sub> and HD column densities. This system has  $[O/H] = -1.43 \pm 0.08$  (Srianand et al. 2000). Thus it appears that the astration factor of deuterium varies largely from one system to the other at a given metallicity. Therefore, it may not be a good idea to remove the so-called outliers while computing the weighted mean value of  $[D/H]$  measured in absorption line systems.

## 6 CONCLUSION

We have presented detailed analysis of two very closely spaced DLAs (at  $z_{\text{abs}}=3.17447$  and  $3.16768$ ) within a velocity separation of  $\sim 500 \text{ km s}^{-1}$  along the line of sight to SDSS J1337+3152. We have reported the detection of 21-cm and molecular hydrogen absorption lines in the damped Lyman- $\alpha$  system at  $z_{\text{abs}}=3.17447$ . This is the second time that both species are detected in the same system. This is a unique combination to constrain at the same time the time variation of the fine structure constant,  $\alpha$ , and the proton-to-electron mass ratio,  $\mu$ . We note however a velocity shift of  $\sim 2.7 \text{ km/s}$  between the H<sub>2</sub> and 21-cm absorption, revealing small scale inhomogeneities in the cloud that could wash out detection of a variation in  $x$ . Such systematics can only be alleviated with a large sample of such systems. However, the redshift of the strongest metal line component matches well with the redshifted 21-cm absorption line. Using this, we derive a stringent limit on the variation of  $x = \alpha^2 g_p / \mu$ ,  $\Delta x/x = -(1.7 \pm 1.7) \times 10^{-6}$ , which is one of the best limits ever obtained. While this demonstrates the advantages of combining GMRT and UVES data, we emphasize the need for a large sample of such measurements.

Using  $N(\text{H I})$  measured from Voigt profile fitting of the damped Lyman- $\alpha$  line in the UVES spectrum together with the 21-cm optical depth measured from our GMRT spectrum, we obtain  $T_s/f_c = 600^{+222}_{-159} \text{ K}$ . This, together with the velocity shift noted above, is consistent with the absorbing gas being a mixture of different phases. We derive mean physical conditions in the cloud,  $U \sim 10^{-3.2}$ ,  $n_{\text{H}} \sim 2 \text{ cm}^{-3}$ ,  $T_{\text{K}} \sim 600 \text{ K}$ . The metallicity is of the order of  $[\text{S}/\text{H}] \sim -1.5$  and the distance to the quasar larger than 270 kpc. We conclude that the gas must be associated with a galaxy in the group or cluster in which the QSO resides.

The gas responsible for the  $z_{\text{abs}}=3.16768$  DLA has very low metallicity,  $[\text{O}/\text{H}] = -2.64 \pm 0.17$ . This allows us to measure the column density of C II accurately. We measure  $[\text{C}/\text{O}] = -0.18 \pm 0.18$ . This means that  $[\text{C}/\text{O}]$  reaches solar value even at very low metallicities. We measure the deuterium abundance in this DLA to be  $\log(\text{D}/\text{H}) = \log(\text{D I}/\text{H I}) = -4.93 \pm 0.15$ . This is a factor of 2 lower than the primordial value,  $[\text{D}/\text{H}]_{\text{p}} = -4.59 \pm 0.02$ , derived from five-year data of the Wilkinson Microwave Anisotropy Probe (WMAP) (Komatsu et al. 2009). We therefore conclude that astration factors can vary significantly even at low metallicity.

## ACKNOWLEDGEMENTS

We thank the GMRT staff for their co-operation during our observations. The GMRT is an international facility run by the National Centre for Radio Astrophysics of the Tata Institute of Fundamental Research. We acknowledge the use of SDSS spectra from the archive (<http://www.sdss.org/>). PN acknowledges the support from the french Ministry of Foreign and European Affairs.

## REFERENCES

Abgrall, H., Roueff, E., Launay, F., & Roncin, J.-Y., 1994, Canadian Journal of Physics, 72, 856

- Akerman, C. J., Carigi, L., Nissen, P. E., Pettini, M., & Asplund, M., 2004, A&A, 414, 931
- Asplund, M., Grevesse, N., Sauval, A. J., & Scott, P., 2009, ARA&A, 47, 481
- Ballester, P., Modigliani, A., Boitquin, O., Cristiani, S., Hanuschik, R., Kaufer, A., & Wolf, S., 2000, The Messenger, 101, 31
- Burles, S. & Tytler, D., 1998, ApJ, 507, 732
- Carilli, C. L. & van Gorkom, J. H., 1992, ApJ, 399, 373
- Chand, H., Srianand, R., Petitjean, P., Aracil, B., Quast, R., & Reimers, D., 2006, A&A, 451, 45
- Chiappini, C., Hirschi, R., Meynet, G., Ekström, S., Maeder, A., & Matteucci, F., 2006, A&A, 449, L27
- Chieffi, A. & Limongi, M., 2002, ApJ, 577, 281
- Cowie, L. L. & Songaila, A., 1995, ApJ, 453, 596
- Crighton, N. H. M., Webb, J. K., Ortiz-Gil, A., & Fernández-Soto, A., 2004, MNRAS, 355, 1042
- Cui, J., Bechtold, J., Ge, J., & Meyer, D. M., 2005, ApJ, 633, 649
- Dekker, H., D’Odorico, S., Kaufer, A., Delabre, B., & Kotzowski, H., 2000, in Proc. SPIE Vol. 4008, p. 534-545, Optical and IR Telescope Instrumentation and Detectors, Masanori Iye; Alan F. Moorwood; Eds., pp. 534-545
- Ferland, G. J., Korista, K. T., Verner, D. A., Ferguson, J. W., Kingdon, J. B., & Verner, E. M., 1998, PASP, 110, 761
- Fox, A. J., Petitjean, P., Ledoux, C., & Srianand, R., 2007, A&A, 465, 171
- Gupta, N., Salter, C. J., Saikia, D. J., Ghosh, T., & Jeyakumar, S., 2006, MNRAS, 373, 972
- Gupta, N., Srianand, R., Petitjean, P., Noterdaeme, P., & Saikia, D. J., 2009, MNRAS, 398, 201
- Hamann, F. & Ferland, G., 1993, ApJ, 418, 11
- Heinmüller, J., Petitjean, P., Ledoux, C., Caucci, S., & Srianand, R., 2006, A&A, 449, 33
- Ivanchik, A., Petitjean, P., Varshalovich, D., Aracil, B., Srianand, R., Chand, H., Ledoux, C., & Boissé, P., 2005, A&A, 440, 45
- Ivanchik, A. V., Petitjean, P., Balashev, S. A., Srianand, R., Varshalovich, D. A., Ledoux, C., & Noterdaeme, P., 2010, ArXiv e-prints
- Kanekar, N. & Chengalur, J. N., 2003, A&A, 399, 857
- Kanekar, N., Subrahmanyam, R., Ellison, S. L., Lane, W. M., & Chengalur, J. N., 2006, MNRAS, 370, L46
- King, J. A., Webb, J. K., Murphy, M. T., & Carswell, R. F., 2008, Physical Review Letters, 101, 251304
- Komatsu, E., Dunkley, J., Nolte, M. R., et al., 2009, ApJS, 180, 330
- Ledoux, C., Petitjean, P., & Srianand, R., 2003, MNRAS, 346, 209
- , 2006, ApJ, 640, L25
- Levshakov, S. A., Dessauges-Zavadsky, M., D’Odorico, S., & Molaro, P., 2002, ApJ, 565, 696
- Markwardt, C. B., 2009, ArXiv e-prints 0902.2850
- Mathews, W. G. & Ferland, G. J., 1987, ApJ, 323, 456
- Moller, P. & Warren, S. J., 1998, MNRAS, 299, 661
- Morton, D. C., 2003, ApJS, 149, 205
- Noterdaeme, P., Ledoux, C., Petitjean, P., & Srianand, R., 2008a, A&A, 481, 327
- Noterdaeme, P., Ledoux, C., Srianand, R., Petitjean, P., & Lopez, S., 2009a, A&A, 503, 765
- Noterdaeme, P., Petitjean, P., Ledoux, C., & Srianand, R.,

- 2009b, *A&A*, 505, 1087
- Noterdaeme, P., Petitjean, P., Ledoux, C., Srianand, R., & Ivanchik, A., 2008b, *A&A*, 491, 397
- Noterdaeme, P., Petitjean, P., Srianand, R., Ledoux, C., & Le Petit, F., 2007, *A&A*, 469, 425
- Petitjean, P., Ledoux, C., & Srianand, R., 2008, *A&A*, 480, 349
- Petitjean, P., Rauch, M., & Carswell, R. F., 1994, *A&A*, 291, 29
- Petitjean, P., Srianand, R., & Ledoux, C., 2000, *A&A*, 364, L26
- Pettini, M. & Bowen, D. V., 2001, *ApJ*, 560, 41
- Pettini, M., Zych, B. J., Murphy, M. T., Lewis, A., & Steidel, C. C., 2008a, *MNRAS*, 391, 1499
- Pettini, M., Zych, B. J., Steidel, C. C., & Chaffee, F. H., 2008b, *MNRAS*, 385, 2011
- Reinhold, E., Buning, R., Hollenstein, U., Ivanchik, A., Petitjean, P., & Ubachs, W., 2006, *Phys. Rev. Lett.*, 96, 151101
- Rodríguez, E., Petitjean, P., Aracil, B., Ledoux, C., & Srianand, R., 2006, *A&A*, 446, 791
- Roy, N., Chengalur, J. N., & Srianand, R., 2006, *MNRAS*, 365, L1
- Sofia, U. J. & Jenkins, E. B., 1998, *ApJ*, 499, 951
- Srianand, R., Noterdaeme, P., Ledoux, C., & Petitjean, P., 2008, *A&A*, 482, L39
- Srianand, R. & Petitjean, P., 1998, *A&A*, 335, 33
- Srianand, R., Petitjean, P., & Ledoux, C., 2000, *Nature*, 408, 931
- Srianand, R., Petitjean, P., Ledoux, C., Ferland, G., & Shaw, G., 2005, *MNRAS*, 362, 549
- Thompson, R. I., Bechtold, J., Black, J. H., et al., 2009, *ApJ*, 703, 1648
- Tubbs, A. D. & Wolfe, A. M., 1980, *ApJ*, 236, L105
- Tzanavaris, P., Webb, J. K., Murphy, M. T., Flambaum, V. V., & Curran, S. J., 2005, *Physical Review Letters*, 95, 041301
- Ubachs, W., Buning, R., Eikema, K. S. E., & Reinhold, E., 2007, *Journal of Molecular Spectroscopy*, 241, 155
- Vanden Berk, D. E., Richards, G. T., Bauer, A., et al., 2001, *AJ*, 122, 549
- Varshalovich, D. A. & Levshakov, S. A., 1993, *Soviet Journal of Experimental and Theoretical Physics Letters*, 58, 237
- Vladilo, G., Centurión, M., D’Odorico, V., & Péroux, C., 2003, *A&A*, 402, 487
- Welty, D. E., Hobbs, L. M., Lauroesch, J. T., Morton, D. C., Spitzer, L., & York, D. G., 1999, *ApJS*, 124, 465
- Wolfe, A. M., Gawiser, E., & Prochaska, J. X., 2005, *ARA&A*, 43, 861
- Wolfire, M. G., McKee, C. F., Hollenbach, D., & Tielens, A. G. G. M., 2003, *ApJ*, 587, 278